

An Intraseasonal Genesis Potential Index for Tropical Cyclones during Northern Hemisphere Summer

JA-YEON MOON

Climate Service and Research Department, Asia–Pacific Economic Cooperation Climate Center, Busan, South Korea

BIN WANG

Department of Atmospheric Sciences, International Pacific Research Center and Atmosphere–Ocean Research Center, University of Hawai‘i at Mānoa, Honolulu, Hawaii, and Earth System Modeling Center, Nanjing University of Information Science and Technology, Nanjing, China

SUN-SEON LEE

Center for Climate Physics, Institute for Basic Science, and Pusan National University, Busan, South Korea

KYUNG-JA HA

Department of Atmospheric Sciences, Division of Earth Environmental System, Pusan National University, Busan, South Korea

(Manuscript received 9 August 2018, in final form 24 August 2018)

ABSTRACT

An intraseasonal genesis potential index (ISGPI) for Northern Hemisphere (NH) summer is proposed to quantify the anomalous tropical cyclone genesis (TCG) frequency induced by boreal summer intraseasonal oscillation (BSISO). The most important factor controlling NH summer TCG is found as 500-hPa vertical motion (ω_{500}) caused by the prominent northward shift of large-scale circulation anomalies during BSISO evolution. The ω_{500} with two secondary factors (850-hPa relative vorticity weighted by the Coriolis parameter and vertical shear of zonal winds) played an effective role globally and for each individual basin in the northern oceans. The relative contributions of these factors to TCG have minor differences by basins except for the western North Atlantic (NAT), where low-level vorticity becomes the most significant contributor. In the eastern NAT, the BSISO has little control of TCG because weak convective BSISO and dominant 10–30-day circulation signal did not match the overall BSISO life cycle. The ISGPI is shown to reproduce realistic intraseasonal variability of TCG, but the performance is phase-dependent. The ISGPI shows the highest fidelity when BSISO convective anomalies have the largest amplitude in the western North Pacific and the lowest when they are located over the north Indian Ocean and eastern North Pacific. Along the NH major TCG zone, the TCG probability changes from a dry to a wet phase by a large factor ranging from 3 to 12 depending on the basins. The new ISGPI for NH summer can simulate more realistic impact of BSISO on TC genesis compared to canonical GPI derived by climatology.

1. Introduction

A new intraseasonal genesis potential index (ISGPI) by Wang and Moon (2017) has been recently proposed to better quantitatively measure the impact of the Madden–Julian oscillation (MJO) on tropical cyclone genesis (TCG) during austral summer (November–April). This new ISGPI significantly improved representation

of intraseasonal variation of TCG in the tropics and each subregion of the Southern Hemisphere (SH). The ISGPI developed for austral summer may not be fully applicable to Northern Hemisphere (NH) TCG because boreal summer intraseasonal oscillation (BSISO) has different propagation, structure, and life cycle from the MJO and the northern oceans have a different land–sea configuration from the southern oceans. Arguably, the quantitative measure for BSISO modulation of TCG during NH summer needs to be separately considered.

Corresponding author: Prof. Bin Wang, wangbin@hawaii.edu

DOI: 10.1175/JCLI-D-18-0515.1

© 2018 American Meteorological Society. For information regarding reuse of this content and general copyright information, consult the [AMS Copyright Policy](https://www.ametsoc.org/PUBSReuseLicenses) (www.ametsoc.org/PUBSReuseLicenses).

Tropical intraseasonal oscillation is a large-scale signal in the atmospheric circulation and deep convection, propagating eastward in a global domain (Madden and Julian 1971, 1972). It displays considerable seasonal variations in their intensity (Madden 1986), frequency (Hartmann et al. 1992), and movement (Lau and Chan 1986; Wang and Rui 1990). Compared to the MJO, which prevails in boreal winter, the BSISO exhibits more complex propagation features (Wang and Rui 1990; Zhu and Wang 1993; Wang and Xie 1996; Annamalai and Slingo 2001; Chu et al. 2017) due to the coexistence of equatorial eastward (Madden and Julian 1971; Hsu et al. 2004) and north/northeastward propagation over the northern Indian Ocean (Yasunari 1979; Kawamura et al. 1996; Wang et al. 2005; Annamalai and Sperber 2005) and northward/northwestward propagation over the western North Pacific (Murakami 1984; Chen and Chen 1993; Kemball-Cook and Wang 2001; Teng and Wang 2003; Jiang et al. 2004; Kajikawa and Yasunari 2005; Yun et al. 2010; Lee et al. 2013). Through the propagating process, the BSISO plays an important role in modulating global-scale tropical–extratropical circulation anomalies (Moon et al. 2013) and severe weather systems such as tropical cyclones (Kikuchi and Wang 2010) or extreme precipitation events over monsoon regions (Hsu et al. 2016).

The evidence of BSISO modulation of TCs was presented as the enhanced activities of TCs at the BSISO's convective phase or the westerly lower-tropospheric wind phase. Possible mechanisms for the BSISO influences on TCs also include reduced vertical wind shear, enhanced low-level convergence and cyclonic relative vorticity, increased midlevel moisture, and small eddies and synoptic disturbances serving as embryos for TCs (Kim et al. 2008; Maloney and Hartmann 2001; Kikuchi and Wang 2010; Huang et al. 2011; Li and Zhou 2013; Crosbie and Serra 2014). Over the northern Indian Ocean (NIO), the BSISO enhances TCG by creating cyclonic vorticity anomaly to the north of the equatorial convection or westerly wind burst (Kikuchi and Wang 2010). Over the western North Pacific (WNP), TCG is clustered near the cyclonic circulation during the westerly phase with an enhanced monsoon trough and a moisture confluent zone (Ko and Hsu 2009; Huang et al. 2011; Kim et al. 2008). When the Western Hemisphere warm pool is established, the influence of BSISO on TCs can be observed (Maloney and Esbensen 2003). The intraseasonal activity significantly alters the low-level wind structure; during the lower tropospheric westerly phase, the wind anomaly helps to provide a favorable condition for TCs to occur in the eastern North Pacific (ENP) and the western part of North Atlantic regions (Maloney and Hartmann 2000a, 2000b; Maloney and

Hartmann 2001; Aiyer and Molinari 2008). Especially, in the main development region (MDR; 10°–20°N, 20°–60°W) of the North Atlantic (NAT), the tropical cyclogenesis is enhanced when the convective phase of BSISO is located over Africa and the western Indian Ocean (Maloney and Shaman 2008; Klotzbach 2010; Ventrice et al. 2011; Klotzbach and Oliver 2015).

Camargo et al. (2009) have first diagnosed the MJO modulation of global tropical cyclogenesis in a quantitative manner. They used the genesis potential index (GPI) developed by Emanuel and Nolan (2004) (hereafter ENGPI) and found that the midlevel relative humidity contributes the largest in MJO modulation of TCG. However, they pointed out that the relationship between the MJO associated anomalies in the GP index and TCG frequency (TCGF) is weaker than the comparable relationship obtained from the climatology. In addition, they applied the same index to both NH summer (August–October) and SH summer (January–March), which does not distinguish the seasonal differences in ISO and TC activity. Klotzbach (2014) demonstrated how tropical cyclones (July–November) in each of the global TC basins are modulated by BSISO. He showed that above-average TCGF, numbers of rapid intensification periods, and accumulated cyclone energy are associated with the convectively enhanced phase of the BSISO; and the primary reason of TCG modulation by BSISO is the changes in large-scale fields, especially reduced vertical shear of zonal wind and enhanced vertical motion. The Atlantic basin was found to have the least phase-by-phase modulation by BSISO.

In the present study, we aim to point out the distinguishing feature of the modulation of TCG by BSISO for NH summer [May–October (MJJASO)]. There are three questions to be specifically addressed. First, what is the most important environmental factor associated with BSISO and how does this factor modulate TCG? Second, how well does the new ISGPI represent BSISO modulation of TCG in the NH summer? Third, what is the main difference compared with ENGPI and the ISGPI for austral summer?

Section 2 briefly describes the datasets and statistical method used in this study. In section 3, the most important large-scale factors through which BSISO controls TCG are presented. A new ISGPI for NH summer is proposed and the commonality and differences of ISGPI among different basins are analyzed in section 4. The performance of ISGPI in representing TCG potential is presented in section 5 and 6, which shows the phase-dependent BSISO modulation (section 5) and regional differences in performance (section 6) compared with ENGPI. The sensitivity in choosing the best matching

BSISO index for deriving ISGPI is discussed in [section 7](#). The last section summarizes the main results and discusses the distinguished difference between the BSISO and the MJO modulations of TCG.

2. Datasets and methodology

a. Datasets

The data used in the present study include daily variables derived from the ERA-Interim reanalysis ([Dee et al. 2011](#)) during 1979–2015. Horizontal resolution is reduced to $2.5^\circ \times 2.5^\circ$ in longitude and latitude. Daily outgoing longwave radiation (OLR) from the National Oceanic and Atmospheric Administration (NOAA) with a horizontal resolution of $2.5^\circ \times 2.5^\circ$ from 1979 to 2015 ([Liebmann and Smith 1996](#)) is used as a proxy to depict convection in the tropics. TC datasets are downloaded from International Best Track Archive for Climate Stewardship (IBTrACS; <http://www.ncdc.noaa.gov/ibtracs>) v03r09 from 1979 to 2015 ([Knapp et al. 2010](#)). TC genesis occurs when it achieves a maximum sustained wind speed of 34 kt (17 m s^{-1}).

Since the boreal summer intraseasonal oscillation prevails during NH summer ([Kikuchi et al. 2012](#); [Lee et al. 2013](#)), the present study focusses on TC season from May to October. A Lanczos bandpass filter ([Duchon 1979](#)) with a cutoff period of 20–70 days is applied to daily datasets and the intraseasonal anomalies are used with the daily climatology removed.

b. A BSISO index for Northern Hemisphere summer

To analyze the modulation of BSISO, we have compared three BSISO indices: the real-time multivariate MJO (RMM) index ([Wheeler and Hendon 2004](#)), the BSISO1 index ([Lee et al. 2013](#)), and a simple OLR index. For the simple OLR index, sensitivity tests have been performed using latitude ranges of 30°S – 30°N , 20°S – 20°N , 15°S – 15°N , 0° – 15°N , 0° – 20°N , and 0° – 30°N . In the EOF analysis, horizontal domains of global tropics with different latitude ranges are applied for the simple OLR index, whereas in the RMM index the 15°S – 15°N averaged global longitude with three variables (OLR and 850- and 200-hPa zonal winds) is used. The BSISO1 index by [Lee et al. \(2013\)](#) was derived in the Asian summer monsoon region (10°S – 40°N , 40° – 160°E) with two variables (OLR and 850-hPa zonal wind). Each of the BSISO indices are obtained by the combination of first two leading principal components during 1979 to 2015 NH summer (MJJASO). Among the BSISO indices, we have selected a simple OLR index with a latitudinal range of 0° – 20°N , which not only

covers the major variability center of BSISO but also shows the highest correlation and consistent relationship with the observed TCG in the NH summer. The resulting two leading EOFs explain 10% and 9% of the total integrated variance, respectively. The lag correlation between the two EOFs has a maximum coefficient of 0.5 at lag day 10 (PC1 tends to lead PC2). The BSISO phase is separated into eight categories and each phase composite is achieved when the amplitude of BSISO index is greater than 1.0 [i.e., $(\text{PC1}^2 + \text{PC2}^2)^{1/2} \geq 1.0$] following [Wheeler and Hendon \(2004\)](#). Comparison of the results derived from the three indices is presented in [section 7](#).

[Figure 1](#) presents the eight-phase evolution of major convection (OLR) anomalies (shading) and TCGF anomalies (contour) by selected BSISO ($\text{OLR}_{0^\circ-20^\circ\text{N}}$) index. The negative enhanced OLR anomalies correspond with increased TCGF anomalies through phases 1 to 8. This relationship is more evident over the WNP and ENP with maximum TCG centered along the 10° – 20°N band. Over the Indian Ocean, the numbers of TCG events are much reduced compared to those in the WNP and ENP because of the enhanced vertical wind shear that develops over the NIO and Indian subcontinent during June to September. In the North Atlantic, TCs tend to evolve in phase with convective anomaly only in the western portion; the BSISO convection anomalies over the MDR (10° – 20°N , 20° – 60°W) in the eastern NAT are very weak and the TCGF anomaly has different periodicity than the BSISO. This weak relationship over the eastern NAT is further discussed in [section 6](#).

c. Method for deriving intraseasonal TC genesis potential index

To derive an ISGPI, we first enlarged the grid size from $2.5^\circ \times 2.5^\circ$ to $10^\circ \times 10^\circ$ grid and used TCGF anomaly at eight composite BSISO phases in order to include as many TCG samples as possible. [Figure 2](#) displays the locations of the TCG during NH summer. The main TC occurrence is found in the latitude belt of 5° – 25°N . The number of boxes covering the TCG locations is 31. These boxes are used to form the statistical samples for deriving the ISGPI with eight BSISO composites, so that the total number of the samples is $31 \times 8 = 248$. Thus, the averaged TCG numbers in each of the $10^\circ \times 10^\circ$ boxed area are sufficient to make meaningful statistics. As indicated in [Fig. 1](#), although the TCGF over the NIO is smaller than other regions, it is included to add more samples. Meanwhile, the samples over the eastern North Atlantic are not used because of their very weak relationship with BSISO.

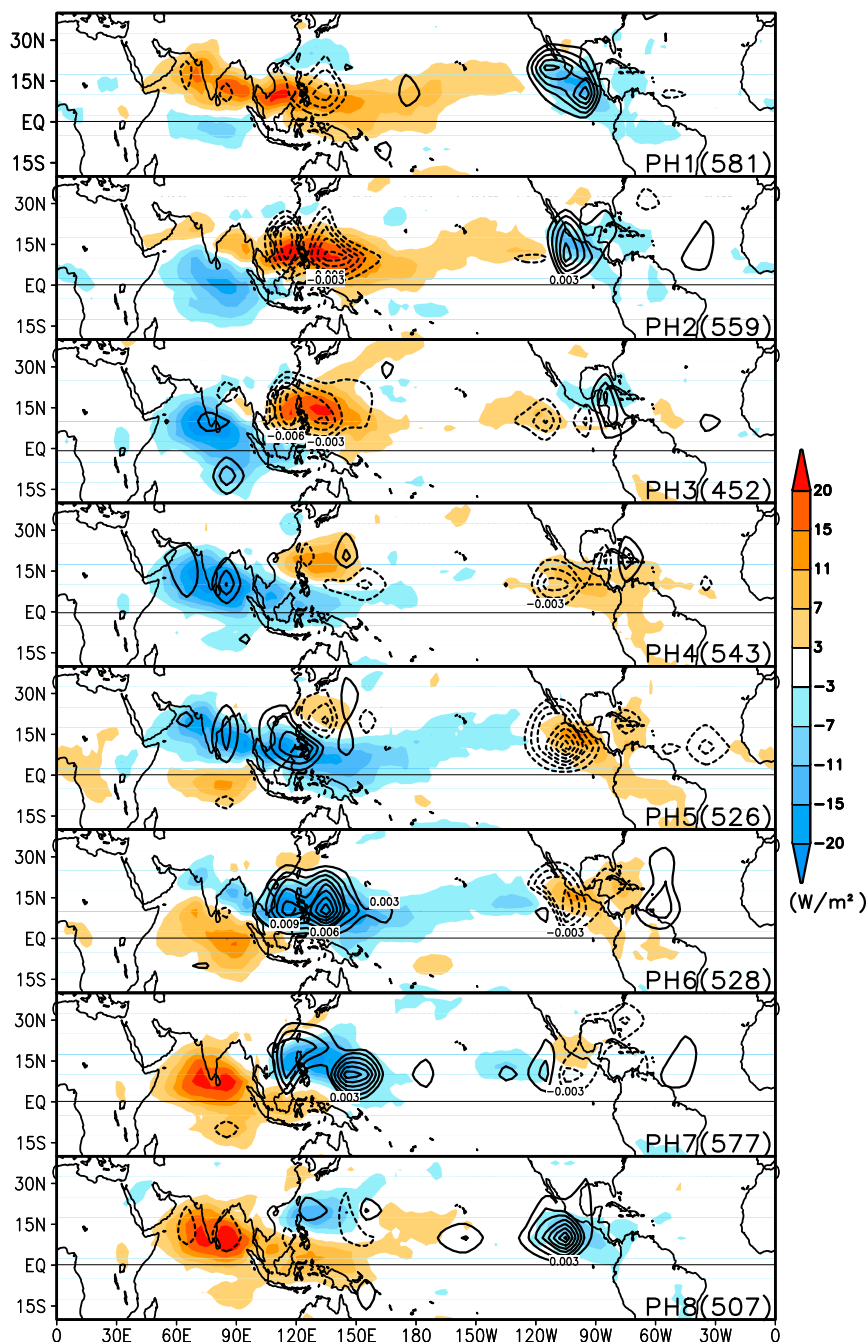


FIG. 1. Eight-phase composite intraseasonal anomalies of OLR (shading) and tropical cyclone genesis frequency (contour, TC number per day) associated with BSISO evolution during Northern Hemisphere summer [May–October (MJJASO)] of 1979–2015. The numbers at the bottom-right corner indicate the total occurrence days at each BSISO phase when the amplitude is greater than 1.0. The BSISO index is obtained by the combination of the first two leading EOF modes using horizontal distribution (0° – 20° N, 0° – 360°) of the MJJASO intraseasonal OLR anomaly.

We used stepwise linear regression and the F test to select the factors and construct the best multivariable linear regression equation. The stepwise regression selects contributing factors in a sequential order by

maximizing the regressed fractional variance at each step (Efroymsen 1960). Fisher's F test was used to test the significance of a new factor at each step in terms of the significance of its contribution to increase of the

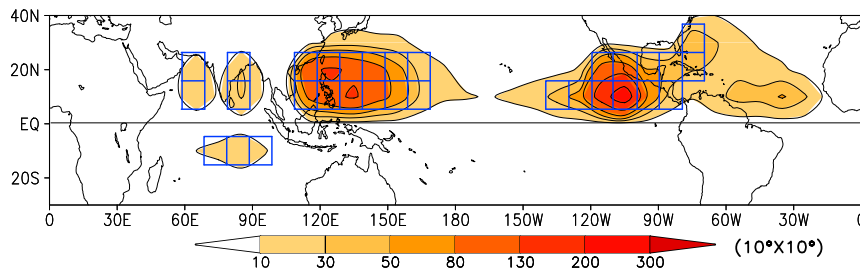


FIG. 2. Total numbers of tropical cyclone genesis events during Northern Hemisphere summer (MJJASO) of 1979–2015. The box indicates the selected $10^{\circ} \times 10^{\circ}$ locations of tropical cyclone genesis for stepwise regression analysis.

regressed variance. At the first step the factor having the highest correlation with TCGF anomaly is selected. At the second step the “newly” selected factor allows for yielding a maximum complex correlation coefficient by its combination with the selected factor. This process continues until no statistically significant factors can be selected.

To evaluate the performance of the new ISGPI, the widely used genesis potential index (GPI) by Emanuel and Nolan (2004) is compared. Since the ENGPI is developed for the total field, we first computed total ENGPI using daily total values (daily climatology + intraseasonal anomaly). Then the ENGPI anomaly on the intraseasonal time scale is obtained by removing the ENGPI climatology (computed using daily climatology values) from the total ENGPI: namely, $\text{ENGPI} = \text{total ENGPI} - \text{climatological ENGPI}$. Different from using the total field variable in ENGPI, the anomalous large-scale environmental factors on an intraseasonal time scale are applied for the new ISGPI. Thus the ISGPI will produce anomalous TC genesis. The performance of new ISGPI for NH summer will be explored and compared with ENGPI in sections 5 and 6.

3. Important factors controlling intraseasonal variation of TC genesis in NH summer

To derive an ISGPI, 10 candidate factors that have been widely used as influential factors for controlling TCG are used, which includes the four factors used in ENGPI, namely the maximum potential intensity (V_{pot} in m s^{-1}), the absolute vorticity at 850 hPa (η_{850} in s^{-1}), the relative humidity at 600 hPa (RH_{600} in percent), and the magnitude of the vertical wind shear between 200 and 850 hPa (V_s in m s^{-1}). Six additional factors are the SST anomaly relative to tropical (30°S – 30°N) mean SST (SST_a), the zonal gradient of the zonal wind at 850 hPa (U_{x850}), the meridional gradient of the zonal wind at 500 hPa (U_{y500}), the vertical shear of the zonal winds between 200 and 850 hPa (V_{zs}),

the relative vorticity at 850 hPa weighted by the Coriolis parameter ($f\zeta_{r850}$), and vertical p velocity at 500 hPa (ω_{500}). These factors are shown to be meaningful factors for TC genesis in the previous studies (Wang and Xie 1996; Latif et al. 2007; Murakami and Wang 2010; Fu et al. 2012). The detailed physical interpretations of each factor are explained in Wang and Moon (2017).

The linear correlations between each individual factor and the observed TCGF anomaly are shown in Table 1. Since the intraseasonal anomaly is used for calculation, the time-independent Coriolis parameter (f) in the absolute vorticity becomes the same as the relative vorticity. The difference between $f\zeta_{r850}$ and ζ_{r850} is the usage of f as a multiplier, which can reduce genesis potential index near the equator and amplify the role of relative vorticity at higher latitudes.

Comparing the correlation coefficients between the TCGF anomaly and 10 candidate factors, it is obvious that ω_{500} has the highest correlation ($R = -0.68$). The V_s , V_{pot} , and SST_a terms show the lowest correlation with the TCG. Both η_{850} and RH_{600} have a close relationship with TCG but their correlations with 500-hPa vertical velocity are very high ($R = -0.74$ and -0.94 , respectively). Disregarding the lowest correlated three variables (V_s , V_{pot} , and SST_a) and the variables that are highly correlated with ω_{500} (η_{850} and RH_{600}), $f\zeta_{r850}$ and V_{zs} seem to be good candidates because they have significant correlations with TCG and are physically more independent of ω_{500} . Although U_{x850} and U_{y500} have higher correlations with TCG than V_{zs} , they are not selected due to their close relationship with ω_{500} .

To understand better the relationship between large-scale environmental factors and the TCG, horizontal distributions of three significantly correlated and relatively independent factors (ω_{500} , V_{zs} , and $f\zeta_{r850}$) and relative humidity (RH_{600}), which has the largest contribution to the ENGPI (Camargo et al. 2009), are plotted in Fig. 3. The convective centers reside in the northeastern ENP and the equatorial Indian Ocean at phase 2 and in the WNP to the central Pacific at phase 6

TABLE 1. Correlation coefficients table among 10 candidate factors and the tropical cyclone genesis frequency (TCGF) anomaly as well as between each of the two candidate factors. The bold numbers indicate statistically significance at the 95% confidence level. Sample size is 248.

	TCGF	V_{pot}	η_{850}	RH_{600}	V_s	SST_a	U_{x850}	U_{y500}	V_{zs}	$f\zeta_{r850}$	ω_{500}
TCGF	1.00	−0.15	0.61	0.61	−0.10	−0.22	−0.45	−0.60	−0.38	0.60	−0.68
V_{pot}	−0.15	1.00	−0.22	−0.01	−0.05	0.72	−0.17	0.24	0.49	−0.34	0.01
η_{850}	0.61	−0.22	1.00	0.69	−0.07	−0.13	−0.39	−0.86	−0.22	0.97	−0.74
RH_{600}	0.61	−0.01	0.69	1.00	−0.05	−0.18	−0.68	−0.63	−0.26	0.61	−0.94
V_s	−0.10	−0.05	−0.07	−0.05	1.00	0.03	0.06	0.03	0.03	−0.06	0.04
SST_a	−0.22	0.72	−0.13	−0.18	0.03	1.00	0.08	0.11	0.56	−0.24	0.16
U_{x850}	−0.45	−0.17	−0.39	−0.68	0.06	0.08	1.00	0.31	0.10	−0.27	0.68
U_{y500}	−0.60	0.24	−0.86	−0.63	0.03	0.11	0.31	1.00	0.33	−0.84	0.69
V_{zs}	−0.38	0.49	−0.22	−0.26	0.03	0.56	0.10	0.33	1.00	−0.30	0.21
$f\zeta_{r850}$	0.60	−0.34	0.97	0.61	−0.06	−0.24	−0.27	−0.84	−0.30	1.00	−0.66
ω_{500}	−0.68	0.01	−0.74	−0.94	0.04	0.16	0.68	0.69	0.21	−0.66	1.00

(Fig. 1). At these two phases, both the intraseasonal anomalies and TCGF anomaly reach maxima over the WNP. The modulation of TCG by BSISO-related large-scale circulation anomalies is clearly displayed

as we can compare the enhanced TCGF anomaly (in contours) with the increased anomalies of ω_{500} , V_{zs} , $f\zeta_{r850}$, and RH_{600} (in shading). At both phases, the maximum enhanced centers of TCGF anomalies match

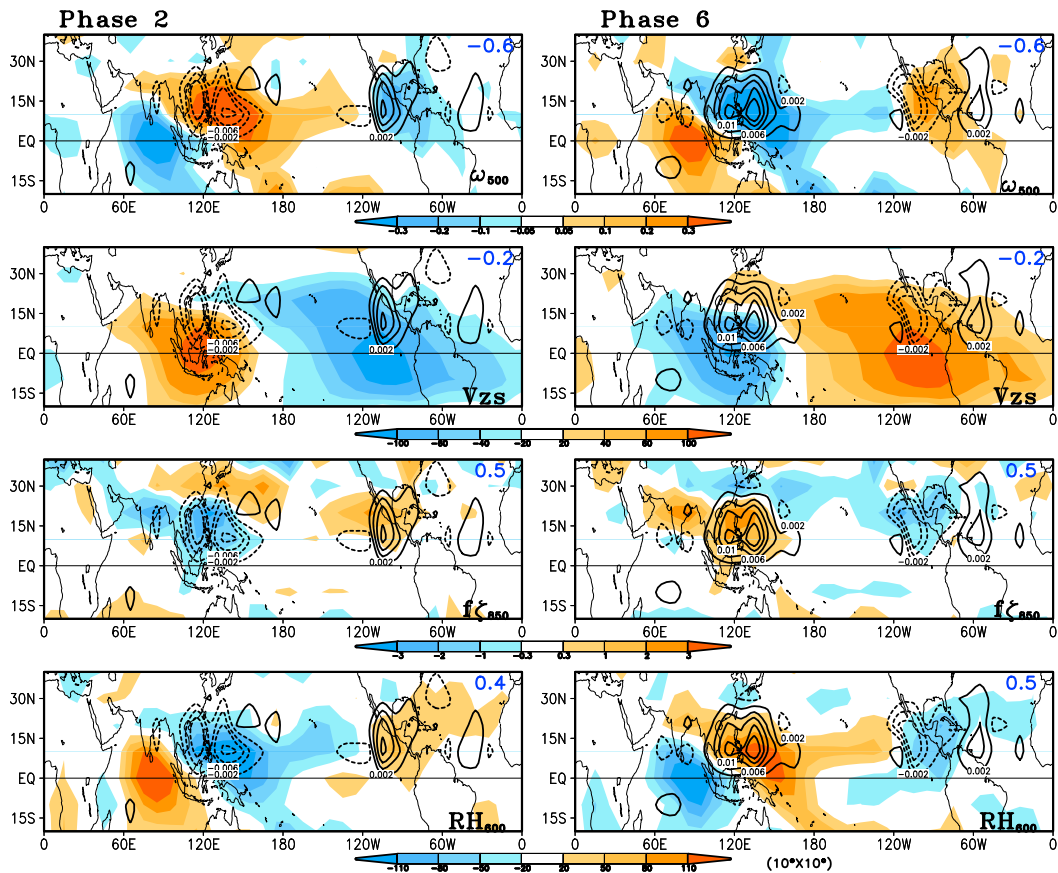


FIG. 3. Composite maps for intraseasonal anomalies of vertical velocity at 500 hPa (ω_{500}), vertical shear of zonal winds (V_{zs}), relative humidity at 600 hPa (RH_{600} ; in shading) at BSISO phases 2 and 6 during Northern Hemisphere summer (MJJASO) of 1979–2015. The tropical cyclone genesis frequency anomaly (TCGF) (number per day) is plotted in black contour; $f\zeta_{r850}$ is scaled by 10^5 . Pattern correlation coefficient between each variable and the TCGF anomaly is shown at the top-right corner.

TABLE 2. Results of stepwise selection of the influential factors for BSISO index. The numbers indicate complex correlation coefficients. The bold number indicates the final complex coefficient by the selected factors. The superscript numbers indicate the order of selection.

BSISO index	V_{pot}	η_{850}	SST_a	RH_{600}	U_{x850}	U_{y500}	V_{zs}	V_s	$f\zeta_{r850}$	ω_{500}
OLR _{0°–20°N}							0.72 ²		0.74 ³	0.68 ¹

the best with those of the negative ω_{500} (upward motion) anomalies at the off-equator regions ($R = -0.6$). Over the Indian Ocean, the ω_{500} anomaly is not correlated with the TCGF anomaly since it is centered at the equator whereas the TCGF centers are in off-equatorial regions. The easterly vertical wind shear favors destabilization of synoptic waves and TC development whereas the westerly vertical wind shear does not (Wang and Xie 1996; Xie and Wang 1996). In both phases, V_{zs} tends to have a longitudinally aligned large-scale pattern and the center is located along the equator. The enhanced TCGF anomaly resides at the periphery of easterly vertical wind shear regions. This longitudinal shift in V_{zs} compared to other factors and TCGF anomaly results in less correlation ($R = -0.2$) compared to ω_{500} or $f\zeta_{r850}$ ($R = 0.4$ – 0.5). Meanwhile, the anomalous distributions of $f\zeta_{r850}$ and RH_{600} correspond well with the TCGF anomaly at the off-equatorial regions.

As shown in horizontal distributions of four environmental factors from Fig. 3, when the BSISO associated intraseasonal anomalies are further shifted toward the NH, the TCG mostly matches with ω_{500} at off-equatorial regions and the $f\zeta_{r850}$ and RH_{600} also correspond well with slightly weaker correlation compared to ω_{500} . Because of the equatorially centered and longitudinally shifted locations, V_{zs} tends to be less correlated with TCG but can play a complementary role as an independent factor.

4. Intraseasonal genesis potential index for NH summer

Analyzing the stepwise regression between the 10 factors and the observed TCGF anomaly, significant influential factors are finally selected and optimized to obtain a best combination of multiple factors (Table 2). The three most influential factors for NH summer TCG are found to be ω_{500} , V_{zs} , and $f\zeta_{r850}$. The complex correlation coefficient of the TCGF anomaly with the three factors is 0.74. With the selected significant factors, the corresponding regressed equation is derived as

$$\text{ISGPI} = (-0.51) \times \omega_{500} + (-0.21) \times V_{zs} + (0.20) \times f\zeta_{r850}.$$

The relative importance of each candidate factor is indicated by the orders of being selected and the

regression coefficients. The latter are normalized for each factor to reflect their relative contributions to the ISGPI. The term ω_{500} has the highest contribution. The $f\zeta_{r850}$ and V_{zs} factors have a comparable weight. Also, V_{zs} is significantly correlated with the TCGF anomaly ($r = -0.38$) and relatively independent from $f\zeta_{r850}$ and ω_{500} . Although RH_{600} , U_{y500} , and U_{x850} have higher correlations with TCGF anomaly than V_{zs} , they are not selected because of their close correlations with ω_{500} or their effects are largely surrogated by ω_{500} .

Since the BSISO has a complex structure in time and space (Kemball-Cook and Wang 2001), each candidate factor may affect differently at each basin. A question arises: Are there differences in the ISGPI among various basins? To answer this question, ISGPI derived by global tropics is compared with the multiregression equations derived for each basin. Separate analyses are conducted for Indian Ocean, WNP, ENP, and western NAT. Only the western part of NAT is considered because the intraseasonal anomalies of large-scale environmental factors have very low correlations with TCGF anomaly in the eastern NAT basin (section 6).

Stepwise regression for each basin revealed commonality in selected influential factors (Table 3). The three important factors in Table 2 (ω_{500} , V_{zs} , and $f\zeta_{r850}$) are consistently selected for each basin. The difference between basins is the order of selection and the relative contribution from each factor. Compared to the global ISGPI, the complex correlation coefficients in the IO, WNP, and ENP are all increased. Over the ENP, it reaches the highest values ($R = 0.84$). This largest correlation is mainly explained by ω_{500} , and V_{zs} played the smallest contribution. Over the IO, the contribution from $f\zeta_{r850}$ is increased and V_{zs} is decreased compared to the global ISGPI. In the WNP, the contributions from three factors remain the same but with a slightly higher R of 0.8. The western NAT showed the least correlation ($R = 0.49$); in contrast to other basins where ω_{500} has the largest contribution, $f\zeta_{r850}$ in the western NAT has the highest contribution and V_{zs} contributes more than ω_{500} . Since the convective activity toward the Western Hemisphere through the NAT becomes weaker and the intraseasonal signal from the upper wind anomaly becomes faster than the convective activity, this environmental change may have a different impact.

TABLE 3. Results of stepwise selection of the influential factors for the BSISO index and the multilinear regression equation for globe and each basin. The numbers indicate complex correlation coefficients. The bold numbers indicate the final complex coefficient by the selected factors at each domain. The superscript numbers indicate the order of selection. The regression coefficients are normalized to reflect their relative contribution.

Region	ω_{500}	V_{zs}	$f\zeta_{r850}$	Equation
Globe	0.68 ¹	0.72 ²	0.74³	$(-0.51) \times \omega_{500} + (0.20) \times f\zeta_{r850} + (-0.21) \times V_{zs}$
IO	0.72 ¹	0.79³	0.78 ²	$(-0.56) \times \omega_{500} + (0.32) \times f\zeta_{r850} + (-0.12) \times V_{zs}$
WNP	0.75 ¹	0.78 ²	0.80³	$(-0.55) \times \omega_{500} + (0.22) \times f\zeta_{r850} + (-0.20) \times V_{zs}$
ENP	0.81 ¹	0.84³	0.84 ²	$(-0.67) \times \omega_{500} + (0.24) \times f\zeta_{r850} + (-0.02) \times V_{zs}$
Western NAT	0.49³	0.48 ²	0.45 ¹	$(-0.16) \times \omega_{500} + (0.46) \times f\zeta_{r850} + (-0.25) \times V_{zs}$

5. Phase-dependent performance of the ISGPI

To analyze how ISGPI represents BSISO modulation of TCG in comparison with the ENGPI, the eight-phase composite maps of the observed TCGF anomaly (shading) and the corresponding ISGPI (contour, left panels) and ENGPI (contour, right panels) are shown in Fig. 4. Each phase is consistent with the convective phase of BSISO in Fig. 1. The TCG is enhanced when the intraseasonal convective anomalies shift to the north of the equator from the equatorial Indian Ocean. Along with the convective anomaly (Fig. 1), the corresponding TCGF anomaly and ISGPI migrate northeastward to the NIO and WNP, then eastward through the ENP to the western NAT. In the eastern part of the NAT, the enhanced TCGF anomaly is found at phases 2–3 and again at phases 6–7, which seems to evolve at a higher frequency different from the BSISO phases.

The major result seen from Fig. 4 is the phase-dependent performance: Both indices have the highest correlation with the TCGF anomaly during phases 2 and 6 and the lowest correlation at phases 4 and 8. During phases 2 and 6, the BSISO convection anomalies have large amplitude both over the WNP and the ENP; the resulting vertical motion anomalies coincide with TCGF anomaly very well. These two basins have the highest TCGF. Thus, the performance at these phases is the best. On the other hand, at phases 4 and 8, the WNP has fewer TCG events and the TCG locations are not captured by the BSISO vertical motion and low-level vorticity anomalies.

Figure 4 also shows that overall, the ISGPI [averaged pattern correlation coefficient (PCC) = 0.64; statistically significant] matches the observed TCGF anomalies much higher than ENGPI (averaged PCC = 0.49; statistically significant). The ENGPI seems to underestimate the signals over the Arabian Sea (phases 4–5) and the southern part of the WNP (phases 6–7). Over the ENP through the Caribbean Sea, the ENGPI has a large discrepancy with the TCGF anomaly in its maximum/minimum peak and the center location.

In sum, the ISGPI for the global Northern Hemisphere consistently and successfully represents intraseasonal

modulation of TCG over the major TC basins, which is significantly better than the ENGPI. Both indices show a phase-dependent modulation of TCG depending on the magnitude and location of the BSISO convective and circulation anomalies. The best performance is found when the BSISO convective anomalies have the largest amplitude in the WNP while the poorest performance is found when the BSISO convective anomalies are located over the NIO and ENP. This phase-dependent regulation of BSISO on TCG calls for our attention when predicting intraseasonal TCG.

6. Regional differences in the performance of the ISGPI

a. Performance by subregion

To examine the performance of the ISGPI at each subregion over the northern oceans, anomalous TCG numbers at each phase of BSISO are represented with the ISGPI and ENGPI in Fig. 5. The tropical cyclone formation at each subregion reveals obvious BSISO modulation when the active phase of BSISO propagates over each domain compared to the suppressed phase. The minimum TCG number can be found at the suppressed phase of BSISO at each subregion. The largest TCG number occurs at phase 4 in the NIO (5°–25°N, 60°–70°E and 80°–90°E), phase 6 in the western part of the WNP (WNPW; 5°–25°N, 110°–130°E), phase 7 in the eastern part of the WNP (WNPE; 5°–25°N, 140°–160°E), phase 1 in the ENP (5°–15°N, 100°–120°W and 15°–25°N, 110°–120°W), and phase 2 in the western NAT (NATW; 5°–15°N, 80°–90°W and 15°–25°N, 70°–100°W). In the eastern NAT (NATE; 5°–15°N, 20°–60°W), there are two peaks of higher frequency at phases 2 and 6.

The ISGPI captures this BSISO regulation of TCG fruitfully over all subregions except for NATE. The maximum peak at each basin corresponds well to the observed TCG. The ENGPI produces a peak with one-phase lag in NIO and WNPW, and a large discrepancy in the ENP basin. Meanwhile, the ENGPI closely reproduced TCG over the WNPE and NATW regions, as did

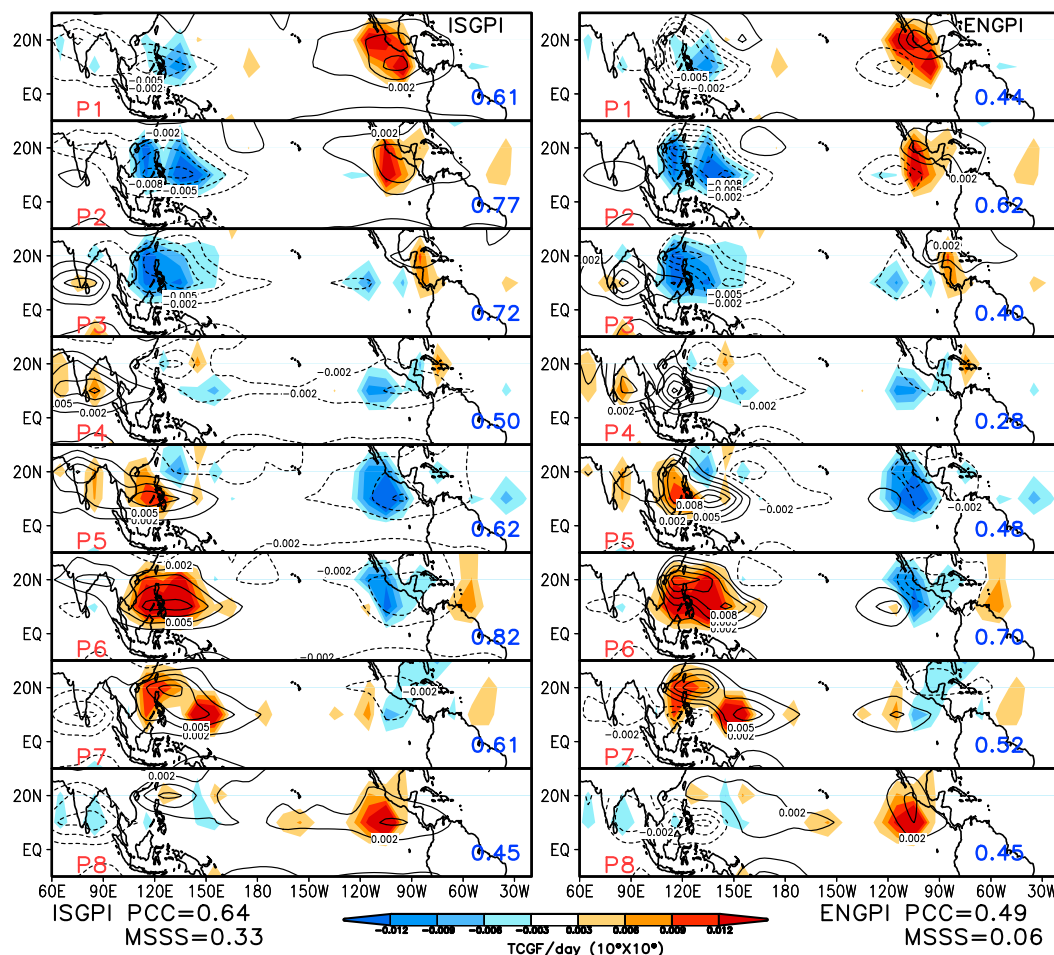


FIG. 4. Performance of the (left) ISGPI (contours) and (right) ENGPI (contours) in reproducing observed tropical cyclone genesis frequency anomaly (color shading) in the Northern Hemisphere during composite eight phases (P1–P8) in MJJASO of 1979–2015. The TCGF anomaly is computed for each day and each $10^{\circ} \times 10^{\circ}$ grid. The numbers at the bottom-right corner of each panel indicate the pattern correlation coefficient (PCC) between each GPI and observed TC genesis frequency anomaly over the (15°S – 25°N , 60°E – 60°W). The average PCC and mean square skill score (MSSS) for eight phases are shown at the bottom of the figure.

the ISGPI. This is because the ENGPI heavily relies on RH_{600} , which tends to have an equatorward shift along with the convective activity near the WNPE region. For the NATW, the correlation coefficient reduces compared to other basins in both ENGPI and ISGPI. Overall, both the mean square skill score (MSSS) and correlation coefficient skills of the ISGPI are significantly higher than the corresponding counterparts of the ENGPI over the NIO, WNPW, and ENP regions.

Figure 6 indicates the probability of TC occurrence at each phase of the BSISO compared to the climatological value over each subregion of the northern oceans. As mentioned in section 2c, ISGPI is derived by anomalous large-scale environmental factors on intraseasonal time scale. The climatology for ISGPI is replaced by the observed TC climatology for this calculation. The TCGF

values in the NIO, WNPW, WNPE, ENP, NATW, and NATE are normalized by their corresponding climatological mean values. Except for NATE, the probability of TCG at each subregion significantly increases at the BSISO convective phase compared to its suppressed phase; note that black contours (TCG) larger than 1.0 tend to shift toward the enhanced phases of BSISO at each location (at phases 4–5 in NIO, phases 5–7 in WNPW, phases 6–7 in WNPE, phases 8–2 in ENP, phases 1–4 in NATW, and phases 2–3 and 6–7 in NATE). In all subregions, the probability of TCG at the convective phase is 1.3–2.4 times higher than the climatological value, while at the suppressed phases the TCG frequency is only 10%–40% of the climatological value.

The ratio of TCG probability between the convective and suppressed phase of BSISO is 12 at NIO, 6 at

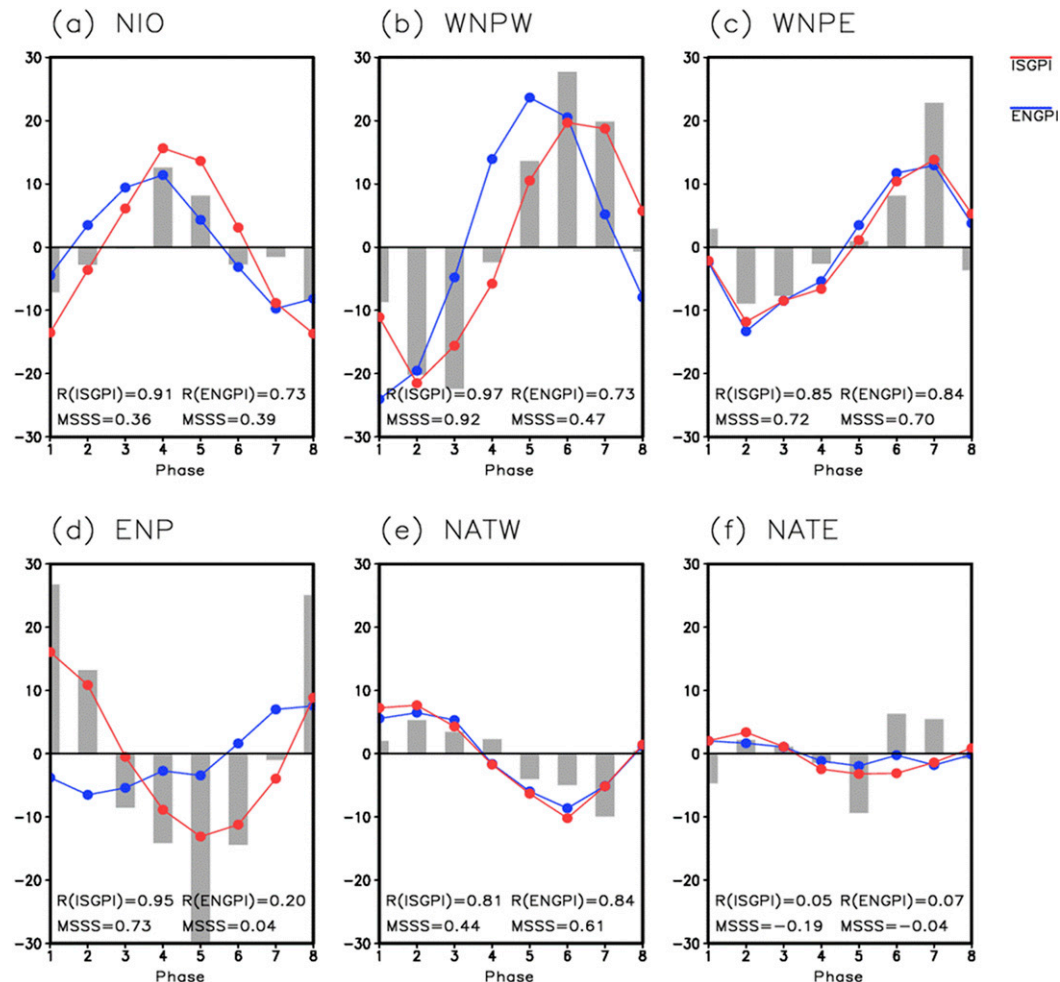


FIG. 5. Performance of the ISGPI (red curves) and ENGPI (blue curves) in reproducing observed TC genesis number (black bar) in six subregions of the northern oceans: the (a) northern Indian Ocean (NIO; 5° – 25° N, 60° – 70° E and 80° – 90° E), (b) western part of western North Pacific (WNPW; 5° – 25° N, 110° – 130° E), (c) eastern part of WNP (WNPE; 5° – 25° N, 140° – 160° E), (d) eastern North Pacific (ENP; 5° – 15° N, 100° – 120° W and 15° – 25° N, 110° – 120° W), (e) western part of North Atlantic (NATW; 5° – 15° N, 80° – 90° W and 15° – 25° N, 70° – 100° W), and (f) eastern part of North Atlantic (NATE; 5° – 15° N, 20° – 60° W) during eight composite phases (P1–P8) of BSISO in NH summer (MJJASO) of 1979–2015. The PCC and MSSS are shown at the bottom of each panel.

WNPW, 3 at WNPE, 5 at ENP, 3 at NATW, and 5 at NATE. The strongest modulation is found in the NIO. Although the number of TCs occurring in the NIO is relatively small, a strong TC in this region could be extremely deadly because of its proximity to dense population areas (Kikuchi and Wang 2010). For NATE, two enhanced phases (Fig. 5) as well as two increased probability phases are found.

From Fig. 6, the robust and strong modulation of BSISO on TCG probability is found. The peak phase and the ratio between the suppressed and the enhanced phases of BSISO at each basin are clearly seen. The BSISO control of TCG probability is better detected in

the ISGPI than the ENGPI, as evidenced by a close match of the red (ISGPI) and black (TCG) curves, suggesting that the probabilistic prediction of TCG can be improved by using the ISGPI.

b. Poor performance over the eastern NAT

Weak modulation of the BSISO on TCG is found over the North Atlantic Ocean with the weak signal of convective activity (Fig. 1) as well as anomalies of the large-scale contributing factors (Fig. 4). Compared to the NATE, the NATW, including the Gulf of Mexico (GoM) and the Caribbean Sea (CS), presents some evidences of BSISO modulation. Several previous studies have

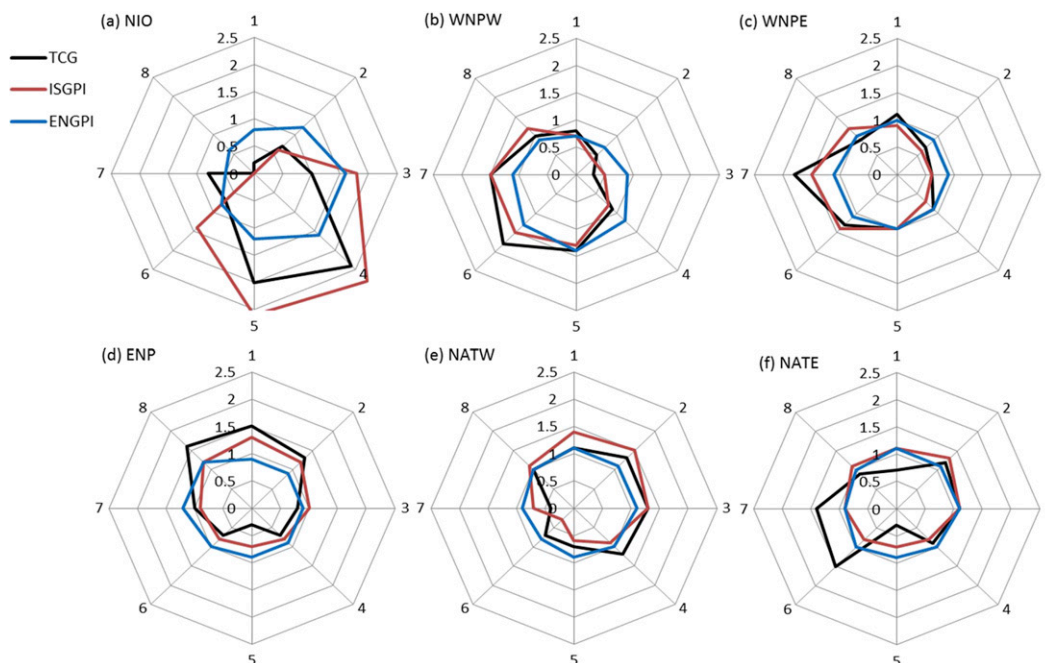


FIG. 6. The normalized TCG frequency (by its corresponding climatological mean TCG frequency at each subregion) during eight composite phases (P1–P8) of BSISO in NH summer (MJJASO) of 1979–2015. Results are derived from observation (black) and predicted by the ISGPI (red) and ENGPI (blue) at six TCG zones in the northern oceans defined as in Fig. 5: the (a) NIO, (b) WNPW, (c) WNPE, (d) ENP, (e) NATW, and (f) NATE.

suggested the strong modulation of TCs by the BSISO in the Atlantic Ocean (Maloney and Hartmann 2000b; Barrett and Leslie 2009; Klotzbach 2010; Klotzbach and Oliver 2015). In Maloney and Hartmann's (2000b) study, the western part of NAT is found to be strongly affected by BSISO. Klotzbach and Oliver (2015) demonstrated major hurricanes in the Atlantic increase when BSISO-related convection is enhanced over Africa and the Indian Ocean (phases 1–3), whereas it is suppressed when the BSISO enhances convection over the western Pacific (phases 5–7). Although other studies argued that the enhanced TC activity over the NAT is associated with increased BSISO convection or upper-level wind, the phase-by-phase relationship is not clearly explained in detail. The possible reasons for this weak modulation of BSISO can be described as follows.

- 1) The close connection of Atlantic TC activity with BSISO may have different results if we consider only tropical cyclone genesis instead of hurricanes or major hurricanes (Klotzbach and Oliver 2015).
- 2) Widely distributed and low density of TCGF at each grid point may disable finding some statistically significant signal over the entire NAT domain.
- 3) Since the intraseasonal signal moves faster in the Western Hemisphere than the Eastern Hemisphere, the BSISO index obtained by global longitudinal

distribution may limit its capability in detecting the proper phase evolution of the BSISO in the NAT region.

- 4) Variations of rainfall and winds over the Atlantic during summer appear to be dominated by two distinct time scales of 10–25 days and 25–60 days (Janicot and Sultan 2001; Sultan et al. 2003; Mounier et al. 2008). To identify the dominant peak of intraseasonal variability over the NAT basin, spectral analysis of the 200-hPa zonal winds is applied to four locations of NAT separately in Fig. 7. At the CS and GoM, the significant 30–80-day spectral peak is stronger than the 10–30-day peak. Meanwhile, the eastern part of the NAT [the MDR and the eastern coast of North America (EC)] has a higher-frequency intraseasonal peak of 10–30 days. The EC has even a high peak around 10 days. This different time scale can be linked to the results in Fig. 5, which show two peaks of TCG numbers over the eastern part of NAT. To better understand and identify the main features over the NAT, further analysis will be needed.

7. Discussion: Sensitivity to choices of BSISO indices

In this section, the sensitivity to the choice of BSISO indices is discussed in order to show how different

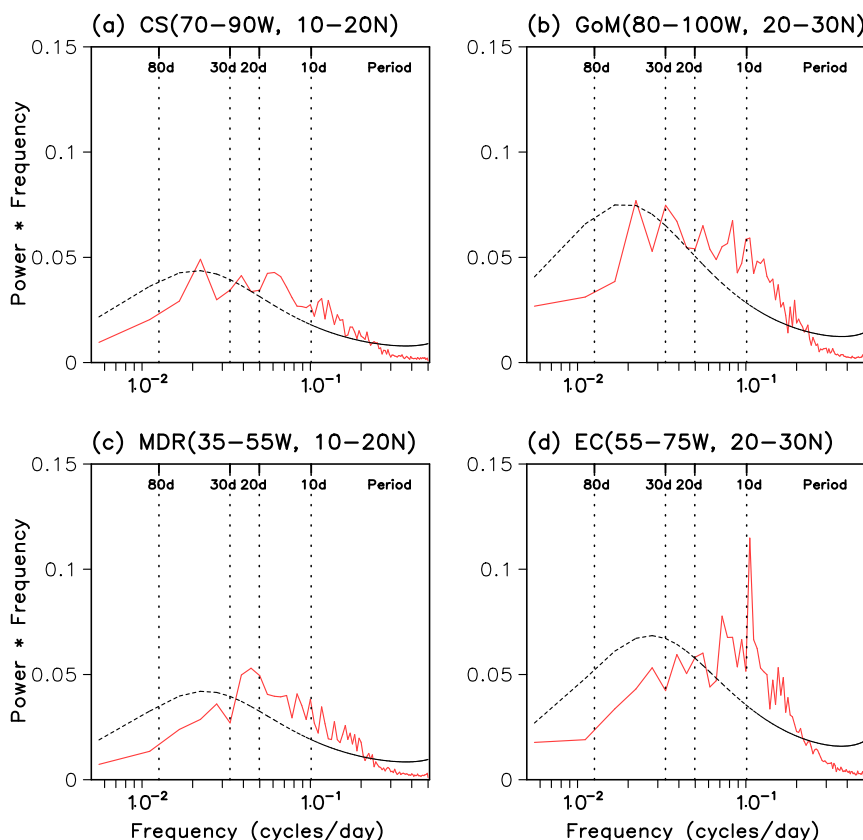


FIG. 7. Power spectra (solid line) of the upper-level (200 hPa) zonal wind anomaly (daily climatology removed) over (a) the Caribbean Sea (10° – 20° N, 70° – 90° W), (b) the Gulf of Mexico (20° – 30° N, 80° – 100° W), and (c) the main development region (MDR; 10° – 20° N, 35° – 55° W) and eastern coast of North America (EC; 20° – 30° N, 55° – 75° W) regions during NH summer (MJJASO) of 1979–2015. The dashed curve is the red-noise spectrum at the 90% confidence level.

BSISO indices distinguish each phase of the BSISO and affect representation of TCG. Table 4 shows the results of stepwise regression by three different BSISO indices. As was described in section 2b, the simple OLR index (0° – 20° N) shows the highest complex correlation coefficient of 0.74. However, considering the values of the correlation coefficients among different indices, there is no significant difference. Among the 10 candidate factors, the BSISO1 index uses the meridional gradient of zonal wind (U_{y500}) instead of $f\zeta_{r850}$ because U_{y500} shows

slightly higher correlation with TCGF anomaly and less correlation with ω_{500} than $f\zeta_{r850}$.

To analyze the differences between the indices in representing the BSISO modulation of TCG, the temporal evolutions of the anomalous TCG numbers with eight BSISO phases in the NIO, WNPW, WNPE, ENP, and WNAT subregions are displayed in Fig. 8. In comparison to the OLR index (as in Fig. 5), the BSISO1 index reproduces higher correlation with GPI only in the WNPW region. The numbers of TCGs in other

TABLE 4. Results of stepwise selection of the influential factors for three BSISO indices: the BSISO1 index (0° – 40° N, 40° – 160° E; OLR and U850), RMM (WH) index (15° S– 15° N, 0° – 360° ; OLR, U200, and U850), and OLR index (0° – 20° N, 0° – 360°). The numbers indicate complex correlation coefficients. The bold numbers indicate the final complex coefficient by the selected factors. The superscript numbers indicate the order of selection.

BSISO index	V_{pot}	η_{850}	SST_a	RH_{600}	U_{x850}	U_{y500}	V_{zs}	V_s	$f\zeta_{r850}$	ω_{500}
BSISO1						0.72 ²	0.73 ³			0.68 ¹
RMM(WH)							0.68 ²		0.70 ³	0.61 ¹
OLR 0° – 20° N							0.72 ²		0.74 ³	0.68 ¹

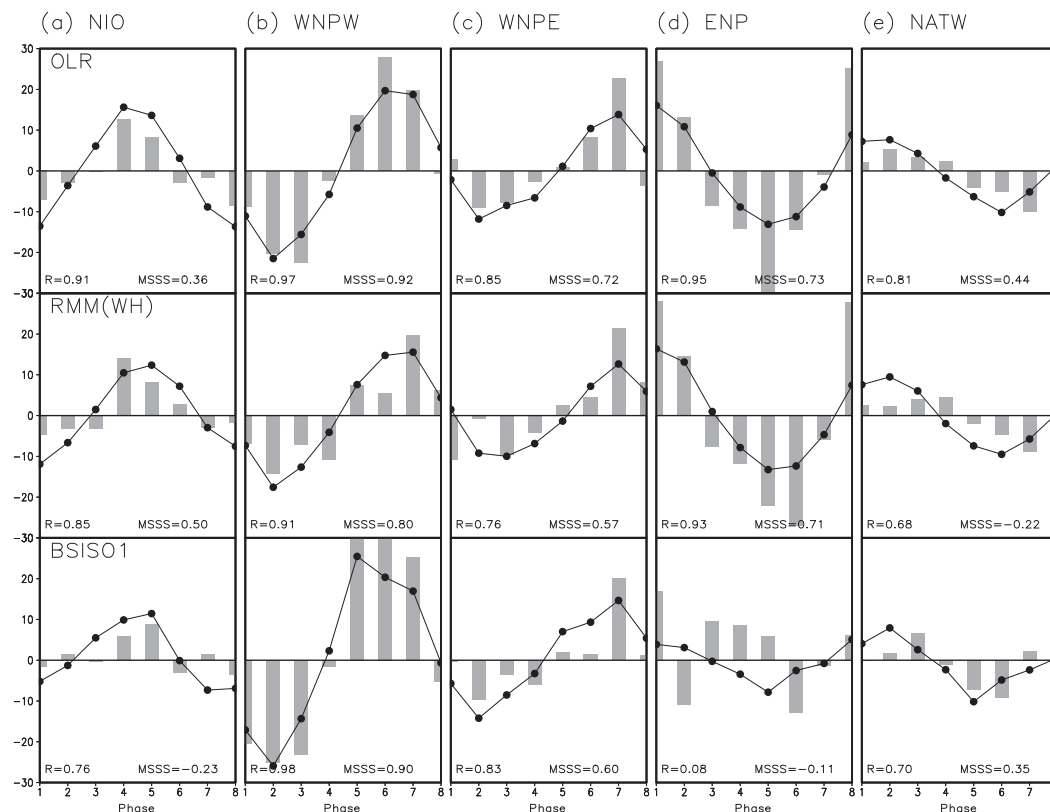


FIG. 8. Performance of the ISGPI (black curves) by three different BSISO indices (OLR, RMM, and BSISO1) in reproducing observed TC genesis number (black bar) in five subregions of the northern oceans, defined as in Fig. 5, the (a) NIO, (b) WNPW, (c) WNPE, (d) ENP, and (e) NATW during eight composite phases (P1–P8) of BSISO in boreal summer (MJJASO) of 1979–2015.

subregions are much less well detected and the BSISO modulation over the ENP is poorly captured. Meanwhile, the RMM index has closer resemblance with the OLR index, but the maximum peak of the TCG numbers are not consistently modulated by the BSISO over the NIO, WNPW, and NATW subregions. The OLR index captures the largest numbers of TCG at each phase of the BSISO with most consistent evolution features with TCG and the large-scale circulation anomalies.

Since the BSISO1 index is obtained from areas of the Asian continent (0° – 40° N, 40° – 160° E), BSISO activity over the WNP (ENP) sector tends to be highlighted well (poorly), resulting in regional differences in representation of global BSISO evolution. The RMM index does not consider the seasonal migration of the convective activity, which may have resulted in weak modulation over the NIO, WNPW, and NATW sectors where the large-scale circulation anomalies associated with BSISO evolution move farther northward.

The derived ISGPI aims to understand the main large-scale factors that control the TCG in boreal summer on

an intraseasonal time scale. The ISGPI is not directly targeted for prediction, although the GPI formula derived here can potentially be used as a component of a hybrid dynamic–empirical prediction model. In this sense, the nature of the ISGPI is similar to the Emanuel–Nolan GPI. The value of this new GPI has been demonstrated through a comparison with the ENGPI using the same dataset.

Derivation of the ISGPI requires a large sample size of training data. The available 35 years of data are marginally sufficient. Because of the limited sample size, we have used all available records to derive the ISGPI and left no suitable data for an independent test. However, such an out-of-sample test is desirable and it should be done when sufficiently large samples of future data become available.

8. Summary

In the present study, a new intraseasonal GPI for anomalous tropical cyclone genesis is proposed for the NH summer during May to October (1979–2015). To

better distinguish eight phases of BSISO, sensitivity test to the choice of proper index is performed. As a result, a simple OLR (0° – 20° N, 0° – 360°) index is selected as the BSISO index (Fig. 1), which yields the highest complex correlation coefficient with tropical cyclone genesis (Table 4), thus capturing the most consistent evolution with the largest numbers of TCG events at each phase. Two other indices, the RMM index by Wheeler and Hendon (2004) and the BSISO1 index by Lee et al. (2013), result in comparable complex correlation coefficients; however, the RMM index showed less consistency in representing the peak phase of TCG over the NIO, western WNP, and western NAT regions and the BSISO1 index captured fewer of TCG events except for in the western WNP and has large discrepancy over the ENP. The deficiencies are largely caused by their definitions in major intraseasonal variability centers: the BSISO1 index focuses mainly over the Asian continent while the RMM index considers intraseasonal variability centered over the equator.

In the NH summer, the most influential large-scale factor controlling tropical cyclone genesis is found to be midtropospheric vertical motion (ω_{500}) (Tables 1 and 2). Two secondary comparable factors are the vertical shear of the zonal winds between 200 and 850 hPa (V_{zs}) and the low-level relative vorticity weighted by the Coriolis parameter ($f\zeta_{r850}$). Different from the austral summer (November–April), the BSISO shifts intraseasonal anomalies northward to the off-equatorial areas where the ω_{500} becomes the most influential factor for TCG, whereas in the austral summer the MJO is trapped at the equator, and the ω_{500} results in a weaker relationship with TCG than $f\zeta_{r850}$ (Wang and Moon 2017).

We proposed a new intraseasonal GPI for NH summer with three most significant contributing factors (Table 2) to quantify the modulation of TCG by BSISO [Eq. (1)]. To find out whether there is any difference in the ISGPI among various basins in the northern oceans, the ISGPI derived for each basin is compared with the global ISGPI (Table 3). As a result, the three important factors (ω_{500} , V_{zs} , $f\zeta_{r850}$) are commonly selected for each basin over the NIO, WNP, ENP, and western NAT. The differences between basins are the relative contribution of each of individual factors. For instance, over the ENP, ω_{500} has a much higher weight whereas V_{zs} has little contribution. In the western NAT, $f\zeta_{r850}$ has the largest but ω_{500} has the least contribution. These changes in contributions may be affected by the localized environmental forcing over the ENP and the weakened convective forcing over the NAT.

The global distribution of the ISGPI successfully quantified intraseasonal variability of TC genesis potential

on each phase of BSISO with an averaged PCC skill of 0.64 (Fig. 4). More importantly, it is found to be phase dependent. When the BSISO convection anomalies become the strongest over the WNP (phases 2 and 6), the ISGPI has the highest correlation with TCG (PCC of 0.77 and 0.82). When the BSISO convection anomalies are over the NIO and ENP with less numbers of TCG over the WNP (phases 4 and 8), the performance becomes the least (PCC of 0.45 and 0.50).

Application of the ISGPI to each subregion of the northern oceans showed high performance capturing the numbers of the observed TCG as well as the ratio of probability between the wettest and driest phases of BSISO (Figs. 5 and 6) for the NIO ($R = 0.91$, MSSS = 0.36), the WNPW ($R = 0.97$, MSSS = 0.92), the WNPE ($R = 0.85$, MSSS = 0.72), the ENP ($R = 0.95$, MSSS = 0.73), and the NATW ($R = 0.81$, MSSS = 0.44). The ratio of TCG probability from the suppressed to the convective phase of BSISO increased to 12 times higher at the NIO, 6 at the WNPW, 3 at the WNPE, 5 at the ENP, 3 at the NATW, and 5 at the NATE.

Of note is the least modulation of TCG ($R = 0.05$, MSSS = -0.19) by BSISO at the NATE, which shows two cycles within the single BSISO cycle (Fig. 5e). Several possible reasons for weak modulation at the NATE region are discussed in this study. The spectral analysis of the upper-level zonal wind for four subregions in the NAT reveals that in the area of the MDR and the eastern coast of North America, a higher-frequency peak (10–30 days) contrasting to the western part (Gulf of Mexico and Caribbean Sea; 30–80 days) is more dominant. This difference in dominant peak between 10–30 and 30–80 days over the eastern NAT perhaps can be the highest possibility for the weak performance (Fig. 7), which leaves further analysis to be explored.

Comparing the performance of the ISGPI with the ENGPI from horizontal distribution (Fig. 4) and TCG numbers and probability for subregions (Figs. 5 and 6), the robust and strong modulation of BSISO on TCG is better detected by the ISGPI. The horizontal distribution of the ENGPI showed less correlated structure of averaged PCC as 0.49 (Fig. 4). In the subregions, the ENGPI produced peak with one phase lag in the NIO and WNPW, and a large discrepancy in the ENP basin (Fig. 5). The ratio of TCGF during the enhanced phase versus the suppressed phase also showed less modulation by the BSISO in the ENGPI (Fig. 6).

The results suggest that the TC genesis index derived from climatology cannot be taken as granted to apply to quantify intraseasonal variation of TCG as many published works have practiced. Second, the results suggest that the mechanism by which the BSISO enhances

TCG is not through reducing vertical shear or increasing maximum potential intensity, as the ENGPI suggested, but rather through enhancing large-scale upward motion and meridional shear of the low-level zonal flows (850-hPa vorticity). Third, the results provide guidance for hybrid dynamic–statistical forecast of the TC genesis; that is, they tell people what types of large-scale field predicted by GCMs can be used to make subseasonal forecasts of TCG. This is what we will further explore. The results also build a basis for further exploration of empirical subseasonal prediction of TCG.

The present study considers only the BSISO modulation of TC genesis and neglects the upscale feedback from TC activity to BSISO. Since the probability of the TCG occurrence is very small and the relative vorticity of TC in its genesis stage is also small, the possible impact of TC itself was found to have little impact (Fig. 6 in Wang and Moon 2017). Considering the more complex behavior of BSISO compared to the MJO in austral summer, use of the ISGPI for NH summer has large potential to improve subseasonal prediction of TC genesis. Further studies are required to understand and identify the relationship between tropical cyclones and the BSISO over the Atlantic.

Because of limited data availability, the performance of the new index was not tested using independent data that are different from the data used to derive the index. It would be useful to make such a rigorous test when the data become available a few years later.

Acknowledgments. This work was supported by NSF Award AGS-1540783 and NOAA Award NA13OAR4310167, the Korea Ministry of Environment (MOE) as “Graduate School specialized in Climate Change,” and by the National Research Foundation of Korea (NRF) through a Global Research Laboratory (GRL) grant (MEST 2011-0021927). This is publication 1347 of IPRC, 10460 of SOEST, and 234 of ESMC of NUIST.

REFERENCES

- Ayyer, A., and J. Molinari, 2008: MJO and tropical cyclogenesis in the Gulf of Mexico and eastern Pacific: Case study and idealized numerical modeling. *J. Atmos. Sci.*, **65**, 2691–2704, <https://doi.org/10.1175/2007JAS2348.1>.
- Annamalai, H., and M. Slingo, 2001: Active/break cycles: Diagnosis of the intraseasonal variability of the Asian summer monsoon. *Climate Dyn.*, **18**, 85–102, <https://doi.org/10.1007/s003820100161>.
- , and K. R. Sperber, 2005: Regional heat sources and the active and break phases of boreal summer intraseasonal (30–50 day) variability. *J. Atmos. Sci.*, **62**, 2726–2748, <https://doi.org/10.1175/JAS3504.1>.
- Barrett, B. S., and L. M. Leslie, 2009: Links between tropical cyclone activity and Madden–Julian oscillation phase in the North Atlantic and northeast Pacific basins. *Mon. Wea. Rev.*, **137**, 727–744, <https://doi.org/10.1175/2008MWR2602.1>.
- Camargo, S. J., M. C. Wheeler, and A. H. Sobel, 2009: Diagnosis of the MJO modulation of tropical cyclogenesis using an empirical index. *J. Atmos. Sci.*, **66**, 3061–3074, <https://doi.org/10.1175/2009JAS3101.1>.
- Chen, T. C., and J. M. Chen, 1993: The 10–20-day mode of the 1979 Indian monsoon: Its relation with the time variation of monsoon rainfall. *Mon. Wea. Rev.*, **121**, 2465–2482, [https://doi.org/10.1175/1520-0493\(1993\)121<2465:TDMOTI>2.0.CO;2](https://doi.org/10.1175/1520-0493(1993)121<2465:TDMOTI>2.0.CO;2).
- Chu, J.-E., B. Wang, J.-Y. Lee, and K.-J. Ha, 2017: Boreal summer intraseasonal phases identified by nonlinear multivariate empirical orthogonal function-based self-organizing map (ESOM) analysis. *J. Climate*, **30**, 3513–3528, <https://doi.org/10.1175/JCLI-D-16-0660.1>.
- Crosbie, E., and Y. Serra, 2014: Intraseasonal modulation of synoptic-scale disturbances and tropical cyclone genesis in the eastern North Pacific. *J. Climate*, **27**, 5724–5745, <https://doi.org/10.1175/JCLI-D-13-00399.1>.
- Dee, D. P., and Coauthors, 2011: The ERA-Interim re-analysis: Configuration and performance of the data assimilation system. *Quart. J. Roy. Meteor. Soc.*, **137**, 553–597, <https://doi.org/10.1002/qj.828>.
- Duchon, C. E., 1979: Lanczos filtering in one and two dimensions. *J. Appl. Meteor. Climatol.*, **18**, 1016–1022, [https://doi.org/10.1175/1520-0450\(1979\)018<1016:LFIOAT>2.0.CO;2](https://doi.org/10.1175/1520-0450(1979)018<1016:LFIOAT>2.0.CO;2).
- Efroymson, M. A., 1960: Multiple regression analysis. *Mathematical Methods for Digital Computers*, A. Ralston and H. S. Wilf, Eds., Wiley, 191–203.
- Emanuel, K. A., and D. S. Nolan, 2004: Tropical cyclone activity and the global climate system. *Proc. 26th Conf. on Hurricanes and Tropical Meteorology*, Miami, FL, Amer. Meteor. Soc., 10A.2, https://ams.confex.com/ams/26HURR/techprogram/paper_75463.htm.
- Fu, B., M. S. Peng, T. Li, and D. E. Stevens, 2012: Developing versus nondeveloping disturbances for tropical cyclone formation. Part II: Western North Pacific. *Mon. Wea. Rev.*, **140**, 1067–1080, <https://doi.org/10.1175/2011MWR3618.1>.
- Hartmann, D. L., M. L. Michelsen, and S. A. Klein, 1992: Seasonal variations of tropical intraseasonal oscillations: A 20–25-day oscillation in the western Pacific. *J. Atmos. Sci.*, **49**, 1277–1289, [https://doi.org/10.1175/1520-0469\(1992\)049<1277:SVOTIO>2.0.CO;2](https://doi.org/10.1175/1520-0469(1992)049<1277:SVOTIO>2.0.CO;2).
- Hsu, H.-H., C.-H. Weng, and C.-H. Wu, 2004: Contrasting characteristics between the northward and eastward propagation of the intraseasonal oscillation during the boreal summer. *J. Climate*, **17**, 727–743, [https://doi.org/10.1175/1520-0442\(2004\)017<0727:CCBTNA>2.0.CO;2](https://doi.org/10.1175/1520-0442(2004)017<0727:CCBTNA>2.0.CO;2).
- Hsu, P.-C., J.-Y. Lee, and K.-J. Ha, 2016: Influence of boreal summer intraseasonal oscillation on rainfall extremes in southern China. *Int. J. Climatol.*, **36**, 1403–1412, <https://doi.org/10.1002/joc.4433>.
- Huang, P., C. Chou, and R. Huang, 2011: Seasonal modulation of tropical intraseasonal oscillation on tropical cyclone genesis in the western North Pacific. *J. Climate*, **24**, 6339–6352, <https://doi.org/10.1175/2011JCLI4200.1>.
- Janicot, S., and B. Sultan, 2001: Intraseasonal modulation of convection in the West African monsoon. *Geophys. Res. Lett.*, **28**, 523–526, <https://doi.org/10.1029/2000GL012424>.
- Jiang, X., T. Li, and B. Wang, 2004: Structures and mechanisms of the northward propagating boreal summer intraseasonal

- oscillation. *J. Climate*, **17**, 1022–1039, [https://doi.org/10.1175/1520-0442\(2004\)017<1022:SAMOTN>2.0.CO;2](https://doi.org/10.1175/1520-0442(2004)017<1022:SAMOTN>2.0.CO;2).
- Kajikawa, Y., and T. Yasunari, 2005: Interannual variability of the 10–25- and 30–60-day variation over the South China Sea during boreal summer. *Geophys. Res. Lett.*, **32**, L04710, <https://doi.org/10.1029/2004GL021836>.
- Kawamura, R., T. Murakami, and B. Wang, 1996: Tropical and mid-latitude 45-day perturbations over the western Pacific during the northern summer. *J. Meteor. Soc. Japan*, **74**, 867–890, https://doi.org/10.2151/jmsj1965.74.6_867.
- Kemball-Cook, S., and B. Wang, 2001: Equatorial waves and air–sea interaction in the boreal summer intraseasonal oscillation. *J. Climate*, **14**, 2923–2942, [https://doi.org/10.1175/1520-0442\(2001\)014<2923:EWAASI>2.0.CO;2](https://doi.org/10.1175/1520-0442(2001)014<2923:EWAASI>2.0.CO;2).
- Kikuchi, K., and B. Wang, 2010: Formation of tropical cyclones in the northern Indian Ocean associated with two types of tropical intraseasonal oscillation modes. *J. Meteor. Soc. Japan*, **88**, 475–496, <https://doi.org/10.2151/jmsj.2010-313>.
- , —, and Y. Kajikawa, 2012: Bimodal representation of the tropical intraseasonal oscillation. *Climate Dyn.*, **38**, 1989–2000, <https://doi.org/10.1007/s00382-011-1159-1>.
- Kim, J., C. Ho, H. Kim, C. Sui, and K. Seon, 2008: Systematic variation of summertime tropical cyclone activity in the western North Pacific in relation to the Madden–Julian oscillation. *J. Climate*, **21**, 1171–1191, <https://doi.org/10.1175/2007JCLI1493.1>.
- Klotzbach, P. J., 2010: On the Madden–Julian oscillation–Atlantic hurricane relationship. *J. Climate*, **23**, 282–293, <https://doi.org/10.1175/2009JCLI2978.1>.
- , 2014: The Madden–Julian oscillation’s impacts on worldwide tropical cyclone activity. *J. Climate*, **27**, 2317–2330, <https://doi.org/10.1175/JCLI-D-13-00483.1>.
- , and E. C. J. Oliver, 2015: Modulation of Atlantic basin tropical cyclone activity by the Madden–Julian oscillation (MJO) from 1905 to 2011. *J. Climate*, **28**, 204–217, <https://doi.org/10.1175/JCLI-D-14-00509.1>.
- Knapp, K. R., M. C. Kruk, D. H. Levinson, H. J. Diamond, and C. J. Neumann, 2010: The International Best Track Archive for Climate Stewardship (IBTrACS): Unifying tropical cyclone data. *Bull. Amer. Meteor. Soc.*, **91**, 363–376, <https://doi.org/10.1175/2009BAMS2755.1>.
- Ko, K.-C., and H.-H. Hsu, 2009: ISO modulation on the sub-monthly wave pattern and recurving tropical cyclones in the tropical western North Pacific. *J. Climate*, **22**, 582–599, <https://doi.org/10.1175/2008JCLI2282.1>.
- Latif, M., N. Keenlyside, and J. Bader, 2007: Tropical sea surface temperature, vertical wind shear, and hurricane development. *Geophys. Res. Lett.*, **34**, L01710, <https://doi.org/10.1029/2006GL027969>.
- Lau, K.-M., and P. H. Chan, 1986: Aspects of the 40–50 day oscillation during the northern summer as inferred from outgoing longwave radiation. *Mon. Wea. Rev.*, **114**, 1354–1367, [https://doi.org/10.1175/1520-0493\(1986\)114<1354:AOTDOD>2.0.CO;2](https://doi.org/10.1175/1520-0493(1986)114<1354:AOTDOD>2.0.CO;2).
- Lee, J. Y., B. Wang, M. C. Wheeler, X. Fu, D. E. Waliser, and I. S. Kang, 2013: Real-time multivariate indices for the boreal summer intraseasonal oscillation over the Asian summer monsoon region. *Climate Dyn.*, **40**, 493–509, <https://doi.org/10.1007/s00382-012-1544-4>.
- Li, R. C. Y., and W. Zhou, 2013: Modulation of western North Pacific tropical cyclone activity by the ISO. Part I: Genesis and intensity. *J. Climate*, **26**, 2904–2918, <https://doi.org/10.1175/JCLI-D-12-00210.1>.
- Liebmann, B., and C. A. Smith, 1996: Description of a complete (interpolated) outgoing longwave radiation dataset. *Bull. Amer. Meteor. Soc.*, **77**, 1275–1277.
- Madden, R. A., 1986: Seasonal variations of the 40–50 day oscillation in the tropics. *J. Atmos. Sci.*, **43**, 3138–3158, [https://doi.org/10.1175/1520-0469\(1986\)043<3138:SVOTDO>2.0.CO;2](https://doi.org/10.1175/1520-0469(1986)043<3138:SVOTDO>2.0.CO;2).
- , and P. Julian, 1971: Detection of a 40–50 day oscillation in the zonal wind in the tropical Pacific. *J. Atmos. Sci.*, **28**, 702–708, [https://doi.org/10.1175/1520-0469\(1971\)028<0702:DOADOI>2.0.CO;2](https://doi.org/10.1175/1520-0469(1971)028<0702:DOADOI>2.0.CO;2).
- , and —, 1972: Description of global-scale circulation cells in the tropics with a 40–50 day period. *J. Atmos. Sci.*, **29**, 1109–1123, [https://doi.org/10.1175/1520-0469\(1972\)029<1109:DOGCC>2.0.CO;2](https://doi.org/10.1175/1520-0469(1972)029<1109:DOGCC>2.0.CO;2).
- Maloney, E. D., and D. L. Hartmann, 2000a: Modulation of eastern North Pacific hurricanes by the Madden–Julian oscillation. *J. Climate*, **13**, 1451–1460, [https://doi.org/10.1175/1520-0442\(2000\)013<1451:MOENPH>2.0.CO;2](https://doi.org/10.1175/1520-0442(2000)013<1451:MOENPH>2.0.CO;2).
- , and —, 2000b: Modulation of hurricane activity in the Gulf of Mexico by the Madden–Julian oscillation. *Science*, **287**, 2002–2004, <https://doi.org/10.1126/science.287.5460.2002>.
- , and —, 2001: The Madden–Julian oscillation, barotropic dynamics, and North Pacific tropical cyclone formation. Part I: Observations. *J. Atmos. Sci.*, **58**, 2545–2558, [https://doi.org/10.1175/1520-0469\(2001\)058<2545:TMJOBOD>2.0.CO;2](https://doi.org/10.1175/1520-0469(2001)058<2545:TMJOBOD>2.0.CO;2).
- , and S. K. Esbensen, 2003: The amplification of east Pacific Madden–Julian oscillation convection and wind anomalies during June–November. *J. Climate*, **16**, 3482–3497, [https://doi.org/10.1175/1520-0442\(2003\)016<3482:TAOEPM>2.0.CO;2](https://doi.org/10.1175/1520-0442(2003)016<3482:TAOEPM>2.0.CO;2).
- , and J. Shaman, 2008: Intraseasonal variability of the West African monsoon and Atlantic ITCZ. *J. Climate*, **21**, 2898–2918, <https://doi.org/10.1175/2007JCLI1999.1>.
- Moon, J.-Y., B. Wang, K.-J. Ha, and J.-Y. Lee, 2013: Teleconnections associated with Northern Hemisphere summer monsoon intraseasonal oscillation. *Climate Dyn.*, **40**, 2761–2774, <https://doi.org/10.1007/s00382-012-1394-0>.
- Mounier, F., S. Janicot, and G. N. Kiladis, 2008: The West African monsoon dynamics. Part III: The quasi-biweekly zonal dipole. *J. Climate*, **21**, 1911–1928, <https://doi.org/10.1175/2007JCLI1706.1>.
- Murakami, H., and B. Wang, 2010: Future change of North Atlantic tropical cyclone tracks: Projection by a 20-km-mesh global atmospheric model. *J. Climate*, **23**, 2699–2721, <https://doi.org/10.1175/2010JCLI3338.1>.
- Murakami, M., 1984: Analysis of deep convective activity over the western Pacific and Southeast Asia. Part II: Seasonal and intraseasonal variations during northern summer. *J. Meteor. Soc. Japan*, **62**, 88–108, https://doi.org/10.2151/jmsj1965.62.1_88.
- Sultan, B., S. Janicot, and A. Diedhiou, 2003: The West African monsoon dynamics. Part I: Documentation of intraseasonal variability. *J. Climate*, **16**, 3389–3406, [https://doi.org/10.1175/1520-0442\(2003\)016<3389:TWAMDP>2.0.CO;2](https://doi.org/10.1175/1520-0442(2003)016<3389:TWAMDP>2.0.CO;2).
- Teng, H., and B. Wang, 2003: Interannual variations of the boreal summer intraseasonal oscillation in the Asia-Pacific region. *J. Climate*, **16**, 3572–3584, [https://doi.org/10.1175/1520-0442\(2003\)016<3572:IVOTBS>2.0.CO;2](https://doi.org/10.1175/1520-0442(2003)016<3572:IVOTBS>2.0.CO;2).
- Ventrice, M. J., C. D. Thorncroft, and P. E. Roundy, 2011: The Madden–Julian oscillation’s influence on African easterly waves and downstream tropical cyclogenesis. *Mon. Wea. Rev.*, **139**, 2704–2722, <https://doi.org/10.1175/MWR-D-10-05028.1>.
- Wang, B., and H. Rui, 1990: Synoptic climatology of transient tropical intraseasonal convection anomalies: 1975–1985. *Meteor. Atmos. Phys.*, **44**, 43–61, <https://doi.org/10.1007/BF01026810>.

- , and X. Xie, 1996: Low-frequency equatorial waves in vertically shear flow. Part I: Stable waves. *J. Atmos. Sci.*, **53**, 449–467, [https://doi.org/10.1175/1520-0469\(1996\)053<0449:LFEWIV>2.0.CO;2](https://doi.org/10.1175/1520-0469(1996)053<0449:LFEWIV>2.0.CO;2).
- , and J.-Y. Moon, 2017: An anomalous genesis potential index for MJO modulation of tropical cyclone. *J. Climate*, **30**, 4021–4035, <https://doi.org/10.1175/JCLI-D-16-0749.1>.
- , P. J. Webster, and H. Teng, 2005: Antecedents and self-induction of active-break South Asian monsoon unraveled by satellites. *Geophys. Res. Lett.*, **32**, L04704, <https://doi.org/10.1029/2004GL020996>.
- Wheeler, M. C., and H. H. Hendon, 2004: An all-season real-time multivariate MJO index: Development of an index for monitoring and prediction. *Mon. Wea. Rev.*, **132**, 1917–1932, [https://doi.org/10.1175/1520-0493\(2004\)132<1917:AARMMI>2.0.CO;2](https://doi.org/10.1175/1520-0493(2004)132<1917:AARMMI>2.0.CO;2).
- Xie, X., and B. Wang, 1996: Low-frequency equatorial waves in vertically sheared zonal flows. Part II: Unstable waves. *J. Atmos. Sci.*, **53**, 3589–3605, [https://doi.org/10.1175/1520-0469\(1996\)053<3589:LFEWIV>2.0.CO;2](https://doi.org/10.1175/1520-0469(1996)053<3589:LFEWIV>2.0.CO;2).
- Yasunari, T., 1979: Cloudiness fluctuations associated with the Northern Hemisphere summer monsoon. *J. Meteor. Soc. Japan*, **57**, 227–242, https://doi.org/10.2151/jmsj1965.57.3_227.
- Yun, K.-S., K.-H. Seo, and K.-J. Ha, 2010: Interdecadal change in the relationship between ENSO and the intraseasonal oscillation in East Asia. *J. Climate*, **23**, 3599–3612, <https://doi.org/10.1175/2010JCLI3431.1>.
- Zhu, B., and B. Wang, 1993: The 30–60 day convection seesaw between the tropical Indian and western Pacific Oceans. *J. Atmos. Sci.*, **50**, 184–199, [https://doi.org/10.1175/1520-0469\(1993\)050<0184:TDCSBT>2.0.CO;2](https://doi.org/10.1175/1520-0469(1993)050<0184:TDCSBT>2.0.CO;2).